Active sites and effects of co-adsorbed  $H_2O$  on isolated methanol dehydrogenation over  $Pt/\gamma$ -  $Al_2O_3$ 

Bryan J. Hare,<sup>1</sup> Ricardo A. Garcia Carcamo,<sup>2,†</sup> Tianjun Xie,<sup>2,†,‡</sup> Paul J. Meza-Morales,<sup>2</sup> Rachel B. Getman,<sup>2</sup> Carsten Sievers<sup>1,\*</sup>

<sup>1</sup>School of Chemical and Biomolecular Engineering, Georgia Institute of Technology, Atlanta, GA 30332

<sup>2</sup>Department of Chemical and Biomolecular Engineering, Clemson University, Clemson, SC 29634

\* Corresponding author: carsten.sievers@chbe.gatech.edu

<sup>†</sup>These authors contributed equally

<sup>‡</sup>Present address: Department of Chemical and Biomolecular Engineering, University of Delaware, Newark, DE 19716

Keywords: aqueous phase reforming, infrared spectroscopy, supported platinum, particle size, solvent effects

#### Abstract

Dehydrogenation is the first reaction of the aqueous phase reforming (APR) mechanism of polyols, and its rate is likely affected by the environment at the active site. This study focuses on reactions of methanol on benchmark  $Pt/\gamma$ - $Al_2O_3$  catalysts probed by infrared spectroscopy under high vacuum. CO in linear and bridging coordination are the dominant surface species on metal sites. Pt particle sizes and reaction temperatures are varied to identify the kinetically preferred active site for methanol dehydrogenation as either lowly coordinated (edges, corners,

interface) or highly coordinated (terraces) metal atoms. Interpretation of temperature-dependent IR spectra up to 450 °C show that larger Pt particles produce more CO at lower temperatures from complete methanol dehydrogenation. Similarly, time-resolved isothermal experiments at 150 °C showed equilibrium conversion occurred much faster on larger Pt particles than smaller ones. Features of evolving v(C=O) bands (shape, vibrational frequencies, integrals) suggest that, even on small Pt particles, CO first forms on the scarcely available terraces, or possibly in the form of islands. We have thus experimentally identified highly coordinated Pt metal as the more active site in overall methanol dehydrogenation. The electronic and chemical effects of co-adsorbed water and hydrogen on dehydrogenation activity and the CO spectra are discussed. The co-adsorption of water, an abundant APR component needed for the water-gas shift reaction, does not appear to affect methanol dehydrogenation on large Pt particles but hinders the reaction on small Pt particles as evident by limited growth in the respective v(C=O) bands.

### Introduction

Hydrogen is one of the most important commodities in the chemical and fuel industries, a climate friendly compound expected to play a key role in the transition from petroleum-based processes to renewable alternatives [1,2]. It remains an essential element for various processes including biomass upgrading [3], ammonia production [4] and Fischer-Tropsch synthesis [5]. In the current state, however, about 96% of H<sub>2</sub> production relies on the processing of non-

renewable resources such as coal, oil, and natural gas [6]. A promising alternative is the utilization of (hemi)cellulosic biomass as a secure, abundant, and renewable source of H<sub>2</sub> [7]. Commonly known methods include direct pyrolysis and gasification of feedstocks as well as reforming of biomass-derived species such as ethanol [8]. However, these processes are energy intensive because they require high temperatures to both vaporize components and surpass energy barriers, while hydrogen yields can be limited due to by-product formation [9]. It is therefore necessary to explore alternative processes to ensure a competitive edge for biorefineries within the future energy industry.

Aqueous phase reforming (APR) has recently garnered much attention as a feasible heterogeneous catalytic process with the potential to produce H<sub>2</sub> directly from biomass-derived oxygenates [10,11]. Possible feedstocks (typically C<sub>x</sub>H<sub>2x+2</sub>O<sub>x</sub> polyols) may vary from smaller species, such as methanol, to larger molecules in low-value feedstocks, such as glycerol and monosaccharides or mixtures of oxygenates that are uneconomical to separate [12-14]. Operating at moderate temperatures (210-250 °C) and continuous flow, APR is notably compatible with conventional biorefinery technologies, capable of direct processing product stream from (hemi)cellulose hydrolysis, and does not require drying or separation of the feedstocks a priori [14-17]. The desired products, H<sub>2</sub> and CO<sub>2</sub>, are gases that can be easily separated from the aqueous reaction medium [18]. Given its potential to produce large H<sub>2</sub> yields, APR has captivated numerous research groups that have since engaged in catalyst screening [19-23], optimization [14,24,25] and reactor design [26,27] aimed at further improving H<sub>2</sub> yields.

Dumesic et al. first reported the conversion of biomass-derived oxygenates dissolved in  $H_2O$  using a  $Pt/Al_2O_3$  catalyst [10]. Theoretically, all of the  $H_2$  can be extracted from these reagents if the dehydrogenation  $\rightarrow$  decarbonylation  $\rightarrow$  water-gas shift reaction sequence is maintained without interference from side reactions. However, the reaction network is controlled by multiple factors that make understanding the mechanism of  $H_2$  production difficult. In practice, the  $H_2$  yield depends on the size of the oxygenate, with larger oxygenates resulting in lower  $H_2$  yields [10]. Additionally, APR is likely structure sensitive, evidenced by the observation that larger Pt particles showed higher  $H_2$  selectivity in glycerol APR without a significant change of the total conversion of glycerol [28]. Thus, a more fundamental understanding of the reactions involved in the APR mechanism is needed, so that improved  $H_2$  production can be achieved.

The APR mechanism may be better understood by studying the type of reaction separately. The first step of the desired reaction sequence is dehydrogenation, which involves breaking C-H and O-H bonds until a catalytically stable intermediate or product is reached [10,29]. Because APR activity is known to be influenced by metal particle size, the dehydrogenation of oxygenates is likely to exhibit an observable dependency as well. Structure sensitivity has been reported for dehydrogenation reactions involving various types of alcohols (aryl, alkyl, etc.) [30-33]. For example, the turnover frequency of benzyl alcohol dehydrogenation on Au/hydrotalcite catalysts increased from ~0.08 to ~0.23 s<sup>-1</sup> as the average Au particle size was decreased from between 4 and 12 to 2.1 nm [30]. It was proposed that metal atoms with low coordination numbers (e.g., edge and corner sites) are much more active

towards alcohol dehydrogenation than those of high coordination (terrace sites) for this particular reaction.

To best isolate the dehydrogenation reaction in a way that is practical for advancing mechanistic knowledge of APR, methanol can be utilized given that it can dehydrogenate but not undergo decarbonylation or side reactions that are prevalent during APR. In a recent computational study, we showed differences in the thermodynamics of C-H and O-H bond cleavage for methanol adsorbed on a Pt(111) terrace and at the interface between a small Pt cluster and a Lewis acidic Al<sub>2</sub>O<sub>3</sub> support [34]. It was determined that Pt terrace sites are generally more active in C-H cleavage while those that are undercoordinated and located at the Pt/Al<sub>2</sub>O<sub>3</sub> interface are more active in O-H cleavage. For the overall dehydrogenation reaction, an experimental approach can further support these findings and provide a better understanding of the particle size effect on the kinetics. However, the dehydrogenation of oxygenates in APR comes with additional complexities. In addition to structural sensitivity, the presence of interfacial H<sub>2</sub>O cannot be ignored. As a co-adsorbate, H<sub>2</sub>O can affect the electronic structure of surrounding metal atoms, compete for surface sites, and solvate adsorbed intermediates or transition states and thus influence cleavage of C-H and O-H bonds [35,36].

To gain fundamental insight into the APR mechanism, methanol conversion on  $Pt/\gamma$ -  $Al_2O_3$  catalysts in high vacuum (HV) was probed by infrared spectroscopy to isolate the dehydrogenation reaction. Pt particle sizes were varied to adjust the ratio of metal sites with different coordination. The features of IR bands (i.e., shapes, integrals, frequencies) corresponding to the adsorbed CO product provided much information during temperature-

dependent and time-resolved experiments regarding the activity of different metal sites along with the effects of co-adsorbed water.

#### Methods

Catalyst synthesis and characterization

1% Pt/γ-Al<sub>2</sub>O<sub>3</sub> was synthesized by wet impregnation. The γ-Al<sub>2</sub>O<sub>3</sub> powder (Alfa Aesar 99.97%) was continuously stirred as a 20 mL aqueous solution of dissolved chloroplatinic acid hydrate, H<sub>2</sub>PtCl<sub>6</sub> (Sigma-Aldrich ≥99.9 trace metals basis), was added in increments with drying and stirring in between. The water for synthesis and experiments was pretreated with a Purelab Classic Elga LabWater deionizer. The impregnated γ-Al<sub>2</sub>O<sub>3</sub> powder was then calcined at 500 °C for 4 h in air prior to reduction at (300, 500, or 700 °C for 3 h in 7% (v/v) H<sub>2</sub>/Ar. Synthesized samples were named in accordance with their reduction temperatures: R300, R500, and R700. The results of the synthesized catalyst were also compared to that of a 5% Pt/ γ-Al<sub>2</sub>O<sub>3</sub> commercial catalyst (Sigma-Aldrich #205974).

An aberration-corrected Hitachi HD 2700 scanning transmission electron microscope (STEM) was used to image supported Pt particles. The resulting high-angle annular dark-field images were acquired with an electron beam convergent angle of 27 mrad and a detector collection angle of 70-370 mrad. Average Pt particle sizes and Pt particle size distributions were determined by manual measurements of 300 – 500 particles per sample.

A Thermo-Scientific Scanning X-ray photoelectron spectrometer (XPS) was used to calculate the surface composition of  $Pt/\gamma$ - $Al_2O_3$  catalysts. Samples were placed under vacuum with pressure below  $4.5 \times 10^{-7}$  mbar. The excitation source utilized focused monochromatic Aluminum K-Alpha X-rays (1.486 keV) with an incident angle of 60 ° normal to the sample. Due to the overlapping of the Pt 4f band by the Al 2p band, surface compositions were calculated with a metal-free basis through manual integrations. Surface compositions were calculated using sensitivity factors of 0.537, 2.93, and 2.285 for the Al 2p, O 1s, and Cl 2p bands [37], respectively, along with the following equation:

$$C_x = \frac{I_x/S_x}{\sum_i I_i/S_i}$$

Where C, I, and S are the surface concentration, orbital band integral, and sensitivity factor of element X, respectively. The carbon peak was centered at 284.4 eV.

A Micromeritics ASAP 2020 analyzer was used for  $N_2$  physisorption and surface area measurements. All samples were initially degassed at 200 °C for 6 hr. The surface area was determined based on the BET method [38].

Pyridine adsorption followed by IR spectroscopy

The Lewis acidity of the catalysts was measured through temperature-programmed desorption of pyridine followed by IR spectroscopy. A Thermo Scientific Nicolet iS10 spectrometer was used to observe pyridine adsorption on catalyst wafers within a HV chamber with the same parameters as the methanol adsorption experiments. Catalyst wafers were

activated at 450 °C for 1 h prior to the incremental dosing of pyridine vapor at 150 °C until the pressure equilibrated at ~0.1 mbar. The HV chamber was evacuated and the same temperature program used for methanol experiments was performed. The strength of acid sites was assessed based on the temperature at with they can retain pyridine under HV. The concentration of Lewis acid sites was calculated with the equation:

$$C_w = \frac{S \times A}{\varepsilon \times W}$$

Where S is the circular area of the catalyst wafer probed by IR spectroscopy, A is the integral of the 1440 cm<sup>-1</sup> band resulting from pyridine adsorption on  $\gamma$ -Al<sub>2</sub>O<sub>3</sub> Lewis acid sites,  $\epsilon$  is an extinction coefficient of 1.71 cm/ $\mu$ mol used for  $\gamma$ -Al<sub>2</sub>O<sub>3</sub> [39], W is the weight of the probed area, and C<sub>w</sub> is the concentration of Lewis acid sites.

# *Infrared spectroscopy*

IR spectroscopy experiments were conducted using a Thermo Scientific Nicolet 8700 FT-IR spectrometer with an MCT/A detector. All spectral data was acquired and processed using Thermo Scientific Omnic software. Infrared spectra were obtained with 64 scans using an aperture of 75, optical velocity of 1.8988, and resolution of 1.928 cm<sup>-1</sup>. Catalyst powders were hydraulically pressed into thin wafers that were placed in a HV chamber with ZnSe windows. Once HV conditions were reached, the catalyst wafer was activated at 450 °C (10 °C/min) for 1 h prior to measuring a spectrum of the pretreated catalyst. The catalyst was then exposed to 0.5 mbar of methanol (VWR International ≥99.8%) vapor at 50 °C and allowed to equilibrate.

For experiments involving methanol adsorption on hydrated catalyst surfaces, the catalyst was exposed to 0.5 mbar of DI water vapor and allowed to equilibrate before dosing methanol. Following another evacuation, the saturated catalyst was then sequentially exposed to temperatures of 150, 250, 350, and 450 °C (10 °C/min) with natural cooling in between to obtain all scans at 50 °C. The spectrum of the dry catalyst surface was subtracted from those with  $H_2O$ - and methanol-derived surface species.

#### Results

# Catalyst characterization

All Pt/ $\gamma$ -Al $_2$ O $_3$  catalysts were characterized to illustrate the impact of various synthesis procedures. The BET surface areas of all catalysts were comparable between 63 and 71 m $^2$ /g, and no significant changes were witnessed with respect to reduction temperature (**Table 1**). Calculated Lewis acidities (**Figure S1**) showed a consistent decrease in acid site concentrations with respect to temperature between different samples. The Lewis acidity of bare  $\gamma$ -Al $_2$ O $_3$  gradually declined from 104  $\mu$ mol/g at 150 °C to 35  $\mu$ mol/g at 450 °C. Those of the Pt/ $\gamma$ -Al $_2$ O $_3$  remained consistently lower ( $\gamma$ 10 – 30  $\mu$ mol/g) due to the obstruction of acid sites (coordinatively unsaturated Al $_3$ + sites [40]) by Pt particles. STEM micrograms (**Figure 1**) verified the increased average particle size with increasing reduction temperature (**Table 1**). Not only do the micrograms reveal high dispersion of Pt nanoparticles across the  $\gamma$ -Al $_2$ O $_3$  surface (for R500 and the commercial catalyst in Figures 1a and 1c, respectively), but also the presence of some single Pt atoms on R300 (**Figure 1a**). Overall, Pt particles on in-house synthesized 1% Pt/ $\gamma$ -

 $Al_2O_3$  catalysts possessed average diameters of 0.5 - 2 nm. These small particles innately possess a large fraction of lowly coordinated Pt sites. On the contrary, the 5% Pt/ $\gamma$ -Al $_2O_3$  commercial catalyst exhibited a much wider distribution of Pt particle sizes from about 2 - 7 nm and an average size that was 3-5 times larger than those of the synthesized samples. Thus, this material contained a large fraction of highly coordinated Pt sites, or terrace sites.

The residual chlorine content from the utilization of  $H_2PtCl_6$  during wet impregnation was measured by XPS on a metal-free basis (**Table 1**). Thus, these atomic percentages should only be considered as a trend between synthesized catalysts. As expected, the residual chlorine content declined with increasing reduction temperature; from 0.64 % at 300 °C to 0 % at 700 °C.

Table 1. Characterization data for  $\gamma$ -Al<sub>2</sub>O<sub>3</sub> and all Pt/Al<sub>2</sub>O<sub>3</sub> catalysts.

Sample	γ-Al <sub>2</sub> O <sub>3</sub>	Synthesized 1% Pt/γ-Al <sub>2</sub> O <sub>3</sub>			Pt/γ-Al <sub>2</sub> O <sub>3</sub>
		R300	R500	R700	com. cat.
Average Pt					
particle size	-	1.0	1.1	1.3	4.6
(nm)					
BET Surface	54	63	71	66	70
Area (m²/g)	34	05	/1	00	70
Cl % (metal	0 %	0.64 %	0.52 %	0.00 %	0.00 %
free basis)	0 %	0.04 //	0.32 //	0.00 %	0.00 %
Actual Pt					
loading (by	-		0.84 %		3.62 %
wt.)					

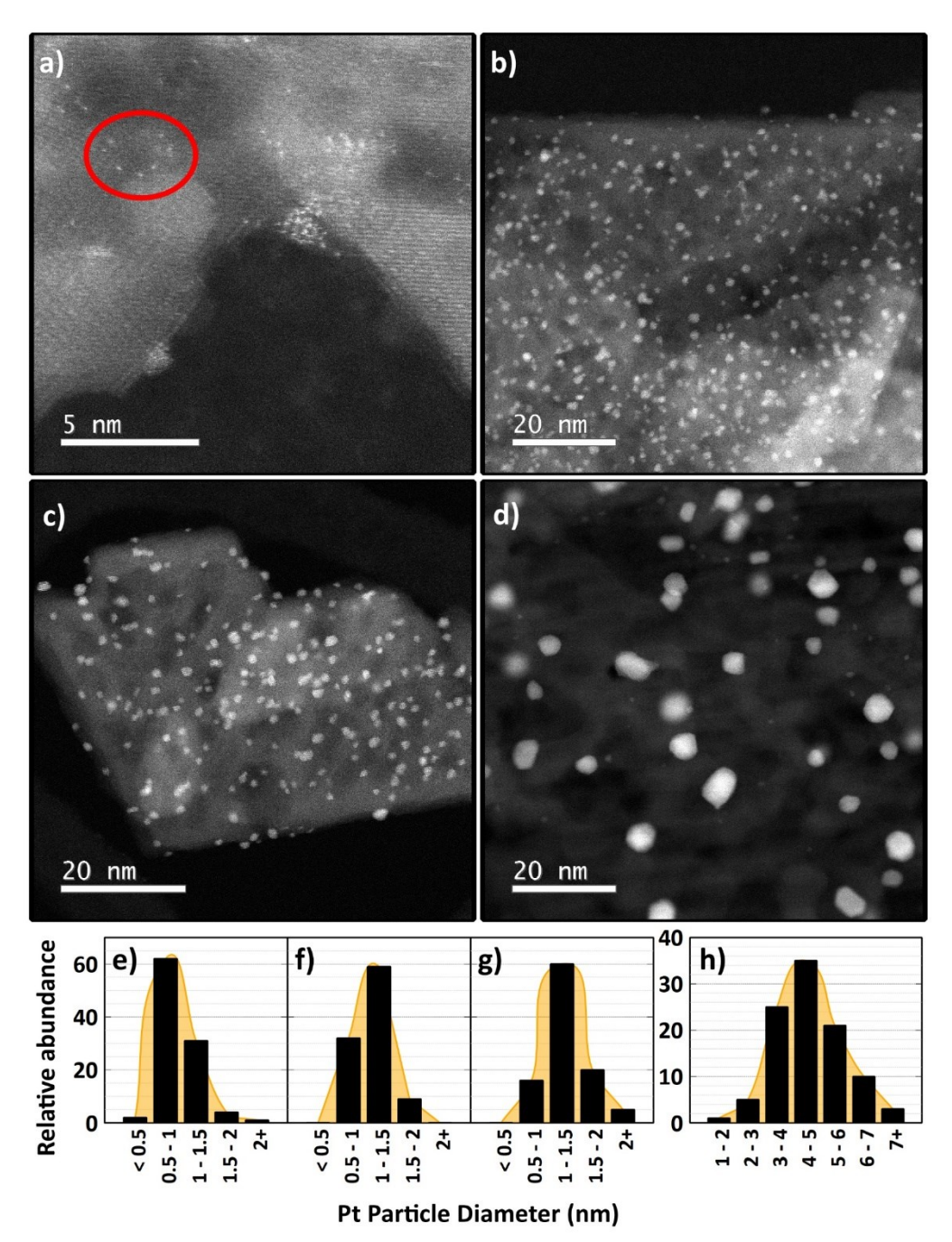


**Figure 1**. STEM micrograms of  $Pt/Al_2O_3$  catalysts. **a)** R300 with a group of single Pt atoms (red oval), **b)** R500, **c)** R700, and **d)** the commercial catalyst. Particle size distributions of **e)** R300, **f)** R500, **g)** R700, and **h)** the commercial catalyst.

Formation of surface species from methanol

The adsorption of methanol on  $\gamma$ -Al<sub>2</sub>O<sub>3</sub> resulted in the emergence of several IR bands (Figure S2 for  $\gamma$ -Al<sub>2</sub>O<sub>3</sub> and Figure S3 for chlorinated  $\gamma$ -Al<sub>2</sub>O<sub>3</sub>). These bands are assigned based on previous work by Busca et al [41]. A broad band at ~3000-3500 cm<sup>-1</sup> represented the  $\nu$ (O-H) modes of hydrogen bonding OH groups from adsorbed methanol and the alumina support. This is accompanied by a group of higher frequency negative bands at 3675, 3732, and 3766 cm<sup>-1</sup> that represent the non-hydrogen bonding surface hydroxyl groups of  $\gamma$ -Al<sub>2</sub>O<sub>3</sub> prior to methanol adsorption [41]. A large band at 1095 cm<sup>-1</sup> was accompanied by smaller high and low frequency shoulders centered at 1190 and 1034 cm<sup>-1</sup>, respectively. These bands were associated with  $\nu$ (C-O) modes of different methanol-derived surface species. Two medium bands with multiple shoulders appeared centralized at 2954 and 2818 cm<sup>-1</sup>. Much of this contribution is due to the asymmetric and symmetric  $\nu$ (CH<sub>x</sub>) modes of different species. Weak bands conglomerated at 1476 and 1420 cm<sup>-1</sup> were due to CH<sub>x</sub> deformations.

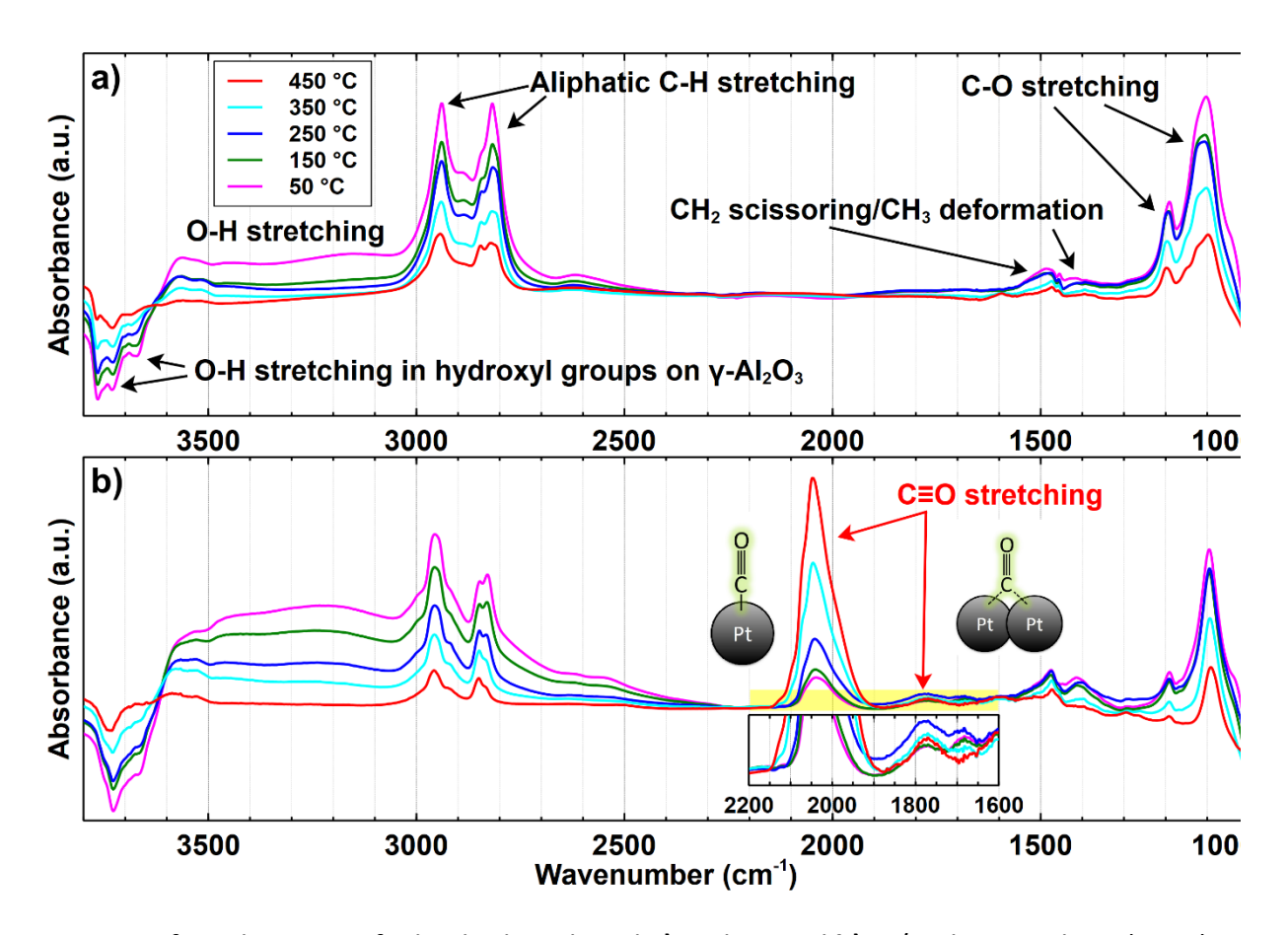


Figure 2. Infrared spectra of adsorbed methanol a)  $\gamma$ -Al<sub>2</sub>O<sub>3</sub> and b) Pt/ $\gamma$ -Al<sub>2</sub>O<sub>3</sub> catalysts (R500) under HV with major vibrational modes labeled. Temperature labels refer to reaction temperature, but all spectra were obtained at 50 °C after allowing the system to cool in ambient air.

The same bands were seen during methanol adsorption on Pt/γ-Al<sub>2</sub>O<sub>3</sub> catalysts (Figure 2). The presence of Pt particles during methanol adsorption resulted in an additional strong band centered at 2048-2080 cm<sup>-1</sup> and a much weaker broad band at 1700-1850 cm<sup>-1</sup> (Figure 2b). These bands were assigned to the stretching modes of CO bound to Pt in the linear (CO<sub>L</sub>) and bridging (CO<sub>B</sub>) coordinations, respectively [42]. The former species typically represents "one-fold" binding, while the latter typically represents two- or three-fold binding. Formation of adsorbed carbon monoxide species indicates complete dehydrogenation of methanol.

Increased temperatures resulted in increased integrals associated with CO with concomitant decreases in the bands affiliated with other methanol-derived species on  $\gamma$ -Al<sub>2</sub>O<sub>3</sub>, indicating higher conversions were achieved at higher temperatures.

# Influence of the Pt particle size

The temperature-dependent evolution of the  $CO_L$  stretching band varied between different Pt/ $\gamma$ -Al $_2O_3$  samples with different metal particle size distributions (Figure 3). These bands maintained a notable broadness throughout the whole temperature range, suggesting that the metal sites exhibit a wide range of coordination and interactions with other elements on the catalyst surface [43,44]. Distinct features were present within the entire range of 1900 – 2150 cm<sup>-1</sup>.

For all synthesized Pt/ $\gamma$ -Al $_2$ O $_3$  samples, the highest intensity was observed within the narrow range of 2048 – 2052 cm $^{-1}$ . For the commercial catalyst, the band centered at 2079 cm $^{-1}$  dominated the region. Each spectrum consisted of a broad low-frequency shoulder that extended as low as 1900 cm $^{-1}$ . The relative intensity of this shoulder became less significant as the Pt particle size increased, suggesting these particular metal sites became less common as metal particles sintered together. We attribute this broad feature to CO $_{L}$  adsorbed near the Pt/ $\gamma$ -Al $_2$ O $_3$  interface with a weaker C $\equiv$ O bond due to interactions with Lewis acid sites [34,45].

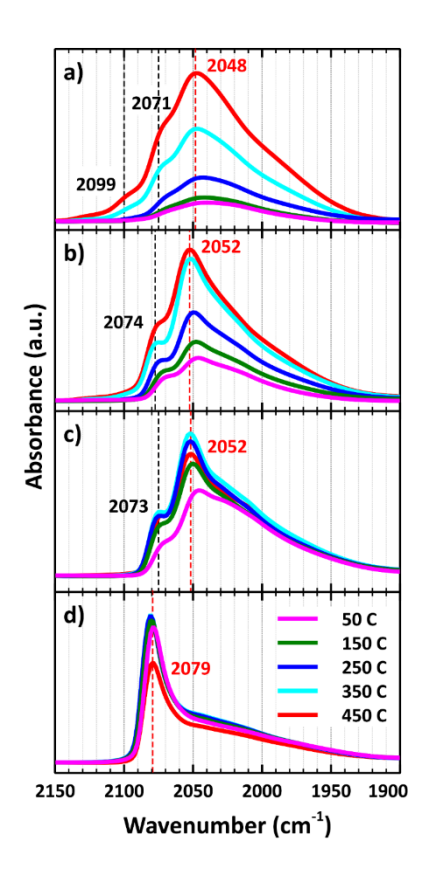


**Figure 3.** CO<sub>L</sub> stretching bands in infrared spectra obtained during temperature-programmed conversion of methanol adsorbed on Pt/ $\gamma$ -Al<sub>2</sub>O<sub>3</sub>: a) R300, b) R500, c) R700, d) commercial catalyst. Absorption band magnitudes are normalized for direct comparison.

The bands for the synthesized Pt/ $\gamma$ -Al $_2$ O $_3$  samples possessed high-frequency shoulders. The shoulder at 2071-2074 cm $^{-1}$  appeared at 250 °C for R300 and as low as 50 °C for R500 and R700. This particular mode appears to correspond to the primary CO $_L$  band of the commercial catalyst, centered at 2079 cm $^{-1}$ . While this band is also associated with CO $_L$  on metal sites, we attributed this slight increase in  $\nu$ (C $\equiv$ O) frequency to dipole-dipole coupling between adjacent adsorbed CO $_L$  species [46]. An additional high frequency shoulder was observed at 2100 cm $^{-1}$  for the R300 and R500 samples. This was more evident for the CO $_L$  band for R300 and was completely absent for the spectra of R700 and the commercial catalyst. One possible

assignment for these particular bands is CO adsorbed on Pt sites that are partially oxidized ( $Pt^{\delta+}$ ) due to residual CI left behind by the  $H_2PtCl_6$  synthesis precursor. CI was completely removed from the surface during reduction at 700 °C as confirmed by XPS, which may explain the absence of the band on spectra for the R700 sample. To further support this assignment, the same methanol dehydrogenation experiment was performed on a sample of R700 that was dosed with HCI to achieve 5 wt. % CI (Figure S4). Not only did the high frequency shoulder emerge with similar intensity as that on R300, but the entire  $CO_L$  band blue-shifted by about 30 cm<sup>-1</sup>. Another possible contribution to these high-frequency bands is CO adsorption on isolated Pt atoms, an assignment made in other studies [47,48]. Single metal atoms could engage in charge transfer with Lewis acidic supports and become slightly oxidized, thus resulting in higher  $v(C\equiv O)$  frequencies [49]. While the STEM micrograms revealed the occasional single Pt atom (Figure 1b), we expect these atoms to sinter with higher reduction temperatures which also explain the disappearance of the band on the spectra for R700. Each of these assignments are further discussed and justified later.

Changes to the  $v(C\equiv O)_L$  frequency with increasing reaction temperature were observed for each Pt/ $\gamma$ -Al $_2$ O $_3$  sample (Figure 4a). For R300, the  $v(C\equiv O)$  band remained low at ~2042 cm $^{-1}$  until the temperature reached 350 °C when it shifted to 2047-2048 cm $^{-1}$ . The  $v(C\equiv O)$  frequency of CO on R500 exhibited a more linear trend, starting at 2046 cm $^{-1}$  at 50 °C and approaching 2052 cm $^{-1}$  at 450 °C. Until 350 °C, the  $v(C\equiv O)_L$  frequency for R700 remained about 2 cm $^{-1}$  higher than that for R500, but it also plateaued at 2052 cm $^{-1}$  above 250 °C. The  $v(C\equiv O)$  frequency for CO $_L$  adsorbed on the commercial catalyst remained at 2080 ±1 cm $^{-1}$  for the whole experiment which is well above that of the synthesized samples (note the y axis break in **Figure 4a**).

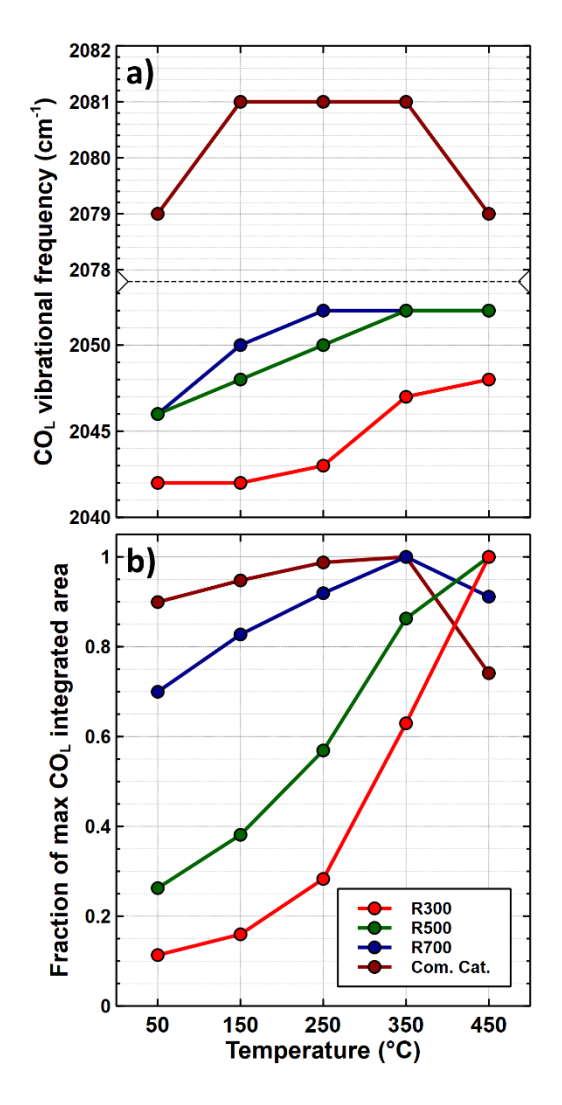


Figure 4. Spectroscopic data for methanol adsorption on various  $Pt/\gamma-Al_2O_3$  catalysts. Changes in a) vibrational frequency and b) integrals of the  $CO_L$  stretching vibrational mode with increasing reaction temperature. The error for  $CO_L$  vibrational frequencies is within ±3 cm<sup>-1</sup>.

The integrals of the cumulative  $CO_L$  bands (i.e.,  $1900-2150 \text{ cm}^{-1}$ ) were obtained at each reaction temperature and plotted as normalized fractions with respect to the maximum area obtained for the respective catalyst sample (Figure 4b). At 50 °C, R300 achieved only 11% of its maximum observed integral. In contrast, the  $CO_L$  band integrals at 50 °C for R500, R700 and the commercial catalyst reached 26, 70, and 90% of their maximum areas, respectively. This

suggests that larger Pt particles, or highly coordinated Pt atoms, are more active in methanol dehydrogenation at lower temperatures. The R700 and commercial catalyst reached their maximum CO<sub>L</sub> integrals at 350 °C, while those with smaller Pt particles required 450 °C.

Effect of adsorbed H<sub>2</sub>O on methanol dehydrogenation

Methanol adsorption experiments were also conducted following exposure of  $Pt/\gamma$ - $Al_2O_3$  catalysts to 0.5 mbar of water vapor. The adsorption of  $H_2O$  resulted in an intensive, broad band within the 2570 – 3660 cm<sup>-1</sup> range due to stretching vibrations of hydrogen bonding OH groups, while the scissoring deformation mode of  $H_2O$  was observed as a medium band at 1646 cm<sup>-1</sup> (**Figure S5**). The spectrum of the hydrated catalyst was subtracted from presented spectra to isolate methanol-derived surface species.  $H_2O$ -derived species, including physisorbed molecular  $H_2O$  within multilayers and surface hydroxyls resulting from dissociative chemisorption, are expected to desorb as the temperature is increased.

The same bands in the 1900-2150 (CO<sub>L</sub>) and 1700-1850 cm<sup>-1</sup> (CO<sub>B</sub>) regions emerged over hydrated Pt/ $\gamma$ -Al $_2$ O $_3$  and dry Pt/ $\gamma$ -Al $_2$ O $_3$  during the adsorption of methanol (Figure 5), demonstrating that methanol dehydrogenation was still achieved in the presence of preadsorbed water. However, for R700 and the commercial catalyst, a few key differences were noted. First, the relative magnitude of the CO<sub>B</sub> band was larger. As a surface species, water is expected to donate electron density the metal hence weakening the C $\equiv$ O bond (vide infra) enough to facilitate to conversion of some CO<sub>L</sub> species to CO<sub>B</sub> [50,51]. This effect was more

pronounced on the commercial catalyst than R700, suggesting that it is easier for adsorbed CO to bind as a bridging species on larger Pt particles.

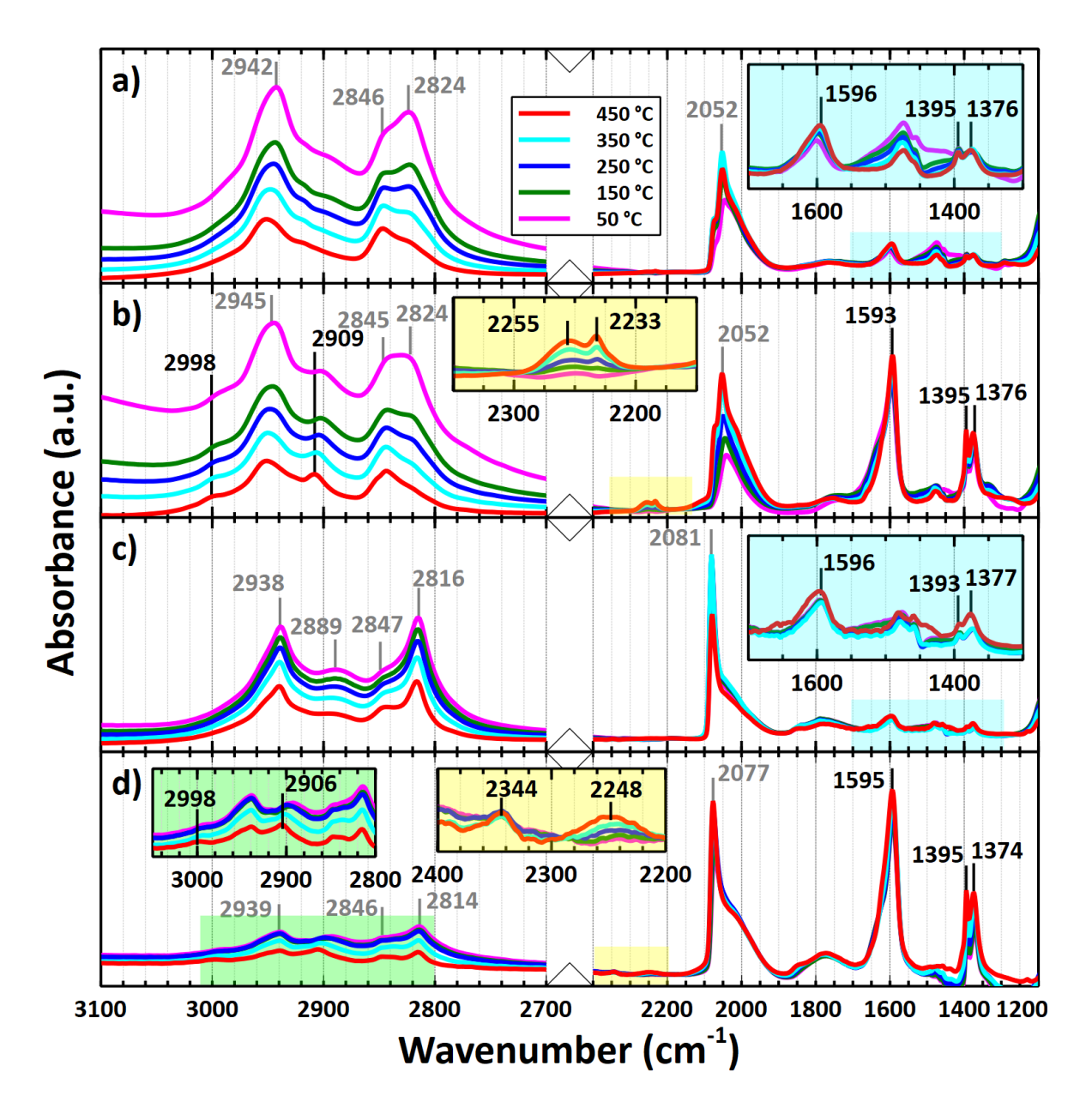


**Figure 5.** IR spectra of temperature-programmed methanol dehydrogenation on Pt/γ-Al<sub>2</sub>O<sub>3</sub> catalysts. **a)** methanol on R700, **b)** methanol/H<sub>2</sub>O on R700, **c)** methanol on the commercial catalyst, and **d)** methanol/H<sub>2</sub>O on the commercial catalyst. Bands with black frequencies are associated with the vibrational modes of a formate species while bands with gray frequencies were assigned to those of species previously identified on dry Pt/γ-Al<sub>2</sub>O<sub>3</sub>.

In addition, a strong band at  $1593 - 1595 \, \mathrm{cm^{-1}}$  was observed in the IR spectra of species on R700 and the commercial catalyst. This represents O-C-O asymmetric stretching mode of a formate species [52]. This is accompanied by additional bands at about 2900 - 2909, 1395, and  $1374 - 1376 \, \mathrm{cm^{-1}}$  representing the C-H stretching, symmetric O-C-O stretching, and O-C-H in plane bending modes of formates [53]. The weak, broad feature centered at  $2998 \, \mathrm{cm^{-1}}$  is believed to arise from the combination of multiple -C-H and =C-H stretching modes in this species [53]. At  $250 \, ^{\circ}$ C, a weak doublet appeared at  $2200 - 2400 \, \mathrm{cm^{-1}}$  and was identified as a  $v_{as}$ (C=O) mode of adsorbed carbon dioxide [54]. This doublet continued to grow slightly with increasing temperature up to  $450 \, ^{\circ}$ C. The spectra of methanol-derived surface species on moisturized catalysts with small Pt particles, R300 and R500 (Figure S6), showed only a weak asymmetric O-C-O stretching band at  $1593 \, \mathrm{cm^{-1}}$  as low as  $150 \, ^{\circ}$ C. There was no evidence of adsorbed carbon dioxide on these samples.

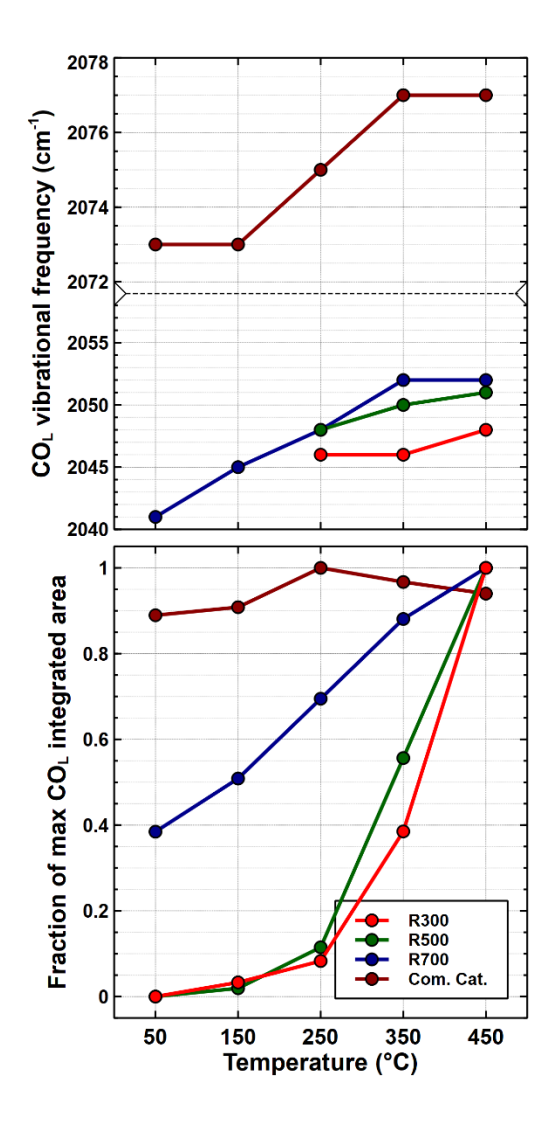


**Figure 6.** Position and fractional peak of the  $CO_L$  stretching peak after methanol adsorption on various hydrated  $Pt/\gamma$ - $Al_2O_3$  catalysts. **a)** vibrational frequency and **b)** integrals of the  $CO_L$  stretching vibrational mode with increasing temperature. The error for  $CO_L$  vibrational frequencies is within  $\pm 3$  cm<sup>-1</sup>.

The vibrational frequencies and integrals of the  $CO_L$  stretching band during methanol dehydrogenation on the  $Pt/\gamma$ - $Al_2O_3$  catalysts (Figure 6) provided insight into the effects of water. As in the experiments without the presence of water, the frequencies increased with temperature. Frequencies were not obtained at 50 and 150 °C for R300 and R500 because there was no evidence of CO formation. By 450 °C, their  $CO_L$  frequencies were 2048 and 2051 cm<sup>-1</sup>,

respectively. Below 150 °C in HV, co-adsorbed water decreased the frequencies of  $CO_L$  on larger Pt particles by 5-8 cm<sup>-1</sup>, in agreement with previous results [55]. In fact, this decrease was consistent amongst every synthesized Pt/ $\gamma$ -Al<sub>2</sub>O<sub>3</sub> sample below 250 °C. The frequencies lined up with those of dry experiments around 350 and 450 °C when much of the H<sub>2</sub>O had desorbed.

In contrast to the lack of CO formation on R300 and R500 at 150 °C and below, the fractional integrals for R700 and the commercial catalyst at 50 °C were 38 and 89 %, respectively. The integral of CO peaks on R300 and R500 demonstrated an exponential conversion trend, reaching their maximum conversion at 450 °C when most of the preadsorbed H<sub>2</sub>O had presumably desorbed. That of R700 was comparatively linear while that of the commercial catalyst was maximized at 250 °C and decreased as the temperature was further increased. While adsorbed CO is a likely source for production of the formate species, consumption of the intermediate on catalysts with large Pt particles did not seem to drastically change the frequency or integral trends.

# Rates of CO Formation

The time-resolved intensities of CO<sub>L</sub> and CO<sub>B</sub> stretching bands on R500 and the commercial catalyst were studied in the presence of 0.5 mbar of methanol vapor at 150 °C (Figure 7). While these Pt particles possess a wide variety of different metal sites, time resolved CO formation can reveal where methanol dehydrogenation occurs preferentially and how quickly the coverage of different Pt particles reaches equilibrium.

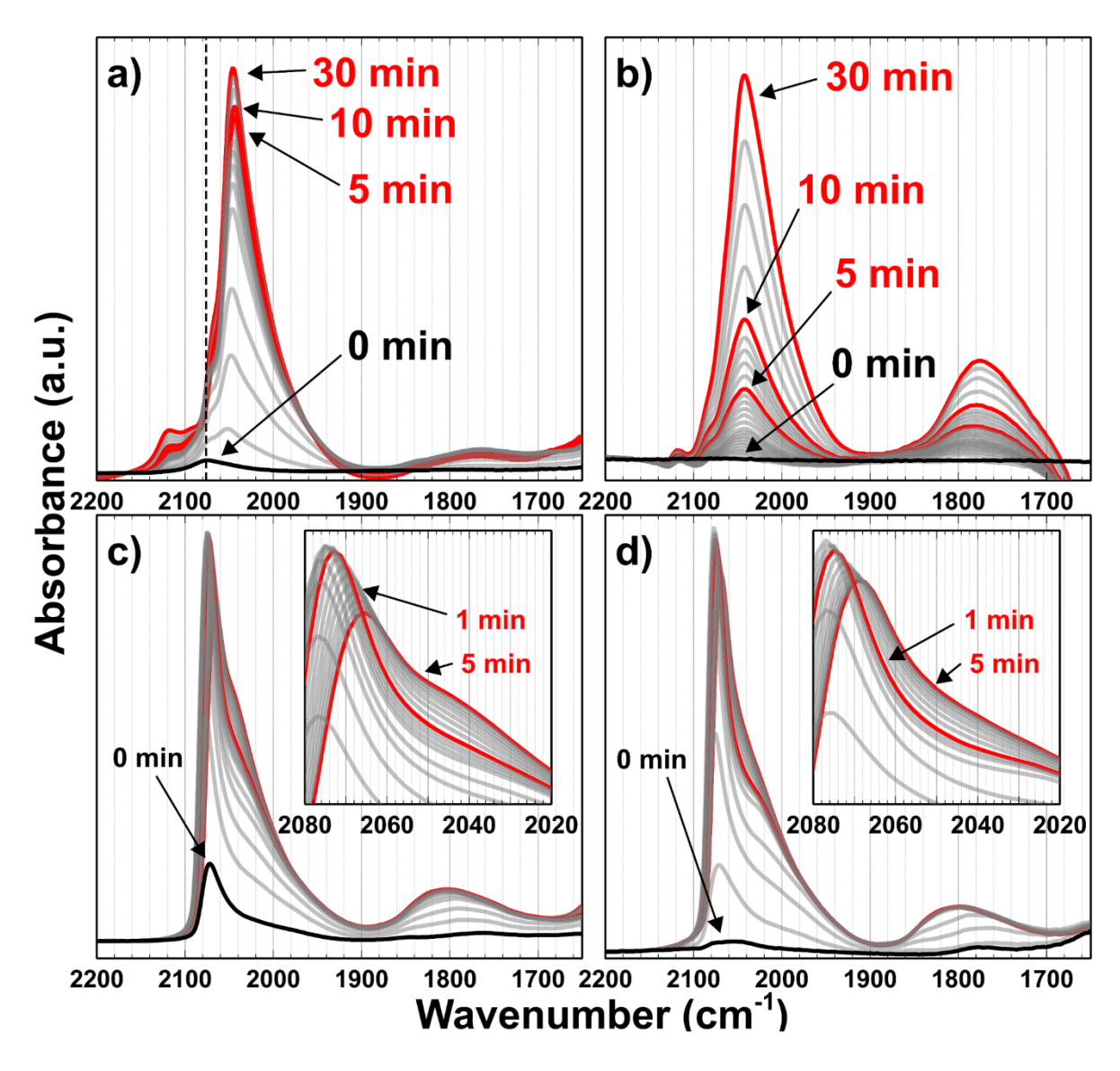


**Figure 7.** CO stretching bands during methanol dehydrogenation on **a)** R500, **b)** R500 preexposed to  $H_2O$  vapor, **c)** the commercial catalyst, and **d)** the commercial catalyst preexposed to  $H_2O$  vapor at 150 °C. Scans were taken as soon as the catalyst was exposed to methanol (black spectra), at time checkpoints once 0.5 mbar of methanol vapor was achieved (red spectra) and time intervals in between checkpoints (gray spectra).

The time for small Pt particles to reach equilibrium dehydrogenation of methanol, or saturation by CO, was about 30 minutes. The  $CO_L$  frequency started at 2076 cm<sup>-1</sup> and ended at

2047 cm<sup>-1</sup> after 30 min. This rate was very slow compared to that of large Pt particles on the commercial catalyst, which seemingly achieved saturation within the first minute and showed an original CO<sub>L</sub> band at 2072 cm<sup>-1</sup>. In addition, the frequency of the CO<sub>L</sub> band on this sample shifted to 2066 cm<sup>-1</sup> after 5 min, while the relative intensity of the low frequency shoulder increased slightly. This supports the kinetic preference of methanol to dehydrogenate on highly coordinated Pt sites over lowly coordinated ones.

For small Pt particles, the presence of water resulted in a remarkable amplification of the CO<sub>B</sub> stretching mode. The growth of this band appeared to be synchronized with that of the CO<sub>L</sub> with both saturating around the same time. In addition, water appeared to impede methanol dehydrogenation on smaller Pt particles given the differences in observed CO<sub>L</sub> integrals at similar times, most notable during the first 10 min. After 5 min, the integral of the CO<sub>L</sub> peak for small, dry Pt particles was about 81% of the value at saturation. For the small Pt particles pre-exposed to water, the corresponding area was only 20 % of its saturated value.

#### Discussion

Interpretation of adsorbed CO spectra

Vibrational modes of adsorbed CO strongly depend on the environment. The vibrational species of  $CO_L$  and  $CO_B$  at 2048-2080 and 1700-1850 cm<sup>-1</sup>, respectively, are much lower than that of gaseous CO at 2143 cm<sup>-1</sup> [56], indicating strong interactions with Pt. The  $CO_L$  species is characterized primarily by strong dative  $\sigma$ -bonds in which electrons from the CO HOMO are donated to the adsorbing Pt atom, while the  $CO_B$  species involves a more extensive degree of  $\pi$ 

back bonding from the metal to the CO antibonding LUMO (and can include two- and threefold coordinate sites on Pt terraces) [57-60]. The vibrational frequency of CO on Pt depends on a combination of electronic (metal atom coordination, oxidation state) [43,47,61,62] and chemical effects (co-adsorbates, solvation) [50,51].

Adsorbed CO is notably sensitive to the coordination of the adsorbing metal atom. It is generally accepted that CO on Pt atoms of higher coordination exhibit higher frequencies and thus stronger C $\equiv$ O bonds [62]. This accounts for the main area of the CO<sub>L</sub> band centered around 2050 cm $^{-1}$ . The large, low-frequency shoulder, extending as low as 1900 cm $^{-1}$ , is unique to CO adsorbed to lowly coordinated metal sites anchored to Lewis acidic supports. In the specific case with Pt/ $\gamma$ -Al $_2$ O $_3$ , it is theorized that the bonding electrons of CO adsorbed near the metal-support interface interact with neighboring Lewis acid sites, thus weakening the CO bond and lowering the  $\nu$ (C $\equiv$ O) frequency [45]. This assignment was confirmed by our recent computational study [34].

Methanol dehydrogenation resulted in a large  $v(C\equiv O)$  band at 2079 cm<sup>-1</sup> on large Pt particles (Figure 3d). This strong band was likely related to the high frequency shoulder centered at 2071 – 2074 cm<sup>-1</sup> seen on the smaller Pt particles. This suggests that an adsorbed CO species of distinct characteristics forms more readily on larger Pt particles, and exhibits limited coverage on smaller particles. We associated this band with the stretching mode of adsorbed CO surrounded by adjacent CO species. When an agglomeration of CO species vibrate in-phase with each other, they engage in dipole-dipole coupling because the orbitals of neighboring CO species interact in a way which further polarizes and strengthens the C=O bond, enlarges the band integral, and increases the stretching frequency [63]. These "CO islands" can

more easily form on larger Pt particles that possess larger terraces, hence the stronger 2079 cm<sup>-1</sup> band seen during methanol dehydrogenation on the commercial catalyst.

The small high frequency shoulders seen above 2100 cm<sup>-1</sup> on R300 and R500 are attributed to adsorbed CO on slightly oxidized Pt sites (Pt<sup>6+</sup>) either from proximity to residual surface CI (from the  $H_2PtCl_6$  precursor) or isolation as single Pt atoms. After deliberately dosing R700, which contained no CI according to XPS (**Table 1**), with 5 wt. % HCl, the high frequency shoulder appeared during methanol dehydrogenation (**Figure S4**). This suggests that some Pt sites were partially oxidized, leading to decreased  $\pi$ -back bonding to adsorbed CO, a stronger C=O bond, and a higher stretching frequency. We believe that the 30 cm<sup>-1</sup> shift of the entire CO<sub>L</sub> peak, also observed in a previous study [64], was due to an electron withdrawing effect due to adsorbed CI near Pt sites. Another contributing factor may be CO bonded to Pt single atoms as noted by other studies [47,66]. These atoms may possess decreased electron density due to direct electron exchange with the support [66]. The extent of  $\pi$ -back bonding to CO would be reduced, justifying the presence of a high frequency shoulder of the CO<sub>L</sub> stretching band. However, the significance of the contribution of this latter species to the high frequency CO<sub>L</sub> stretching band remains to be quantified.

Pt particle size effects on dehydrogenation activity

The metal particle size of a supported catalyst correlates directly with the speciation of metal sites on the surface. Large metal particles have more highly coordinated terrace sites compared to the larger abundancy of edges, corners, and kinks on small metal particles. These

different sites are expected to exhibit different reactivity due to differences in their electronic structures and sterics of adsorbed species [68]. The R300, R500, and R700 samples had average Pt particle sizes of 1.0, 1.1, and 1.3 nm, respectively, with different overall size distributions. Comparing these to the commercially obtained  $Pt/\gamma$ -Al<sub>2</sub>O<sub>3</sub> catalyst with an average Pt particle size of 4.6 nm and a wide size distribution was an efficient way to study the reactivity of metal sites with different coordination.

The present IR spectra of adsorbed CO formed by methanol dehydrogenation give insight into the reactivity of active sites (Figures 2 and 3). The prominent C=O stretching modes for all catalysts with Pt particle sizes as small as 0.5 nm and as large as 7+ nm (Table 1) showed that methanol dehydrogenation may proceed on a variety of metal sites. However, corroborating trends between Pt particle size and certain features of the CO<sub>L</sub> band imply that highly coordinated Pt sites are preferred for dehydrogenation. For instance, larger CO<sub>L</sub> band integrals (i.e., higher conversions) were observed on catalysts with larger Pt particles at lower temperatures (Figure 4b). However, the differences in  $\nu$ (C=O) integrals with respect to Pt particle size become less significant with increasing metal particle size. At 50 °C, a 132% difference was observed between R300 and R500 (average Pt particle sizes of 1.0 and 1.1, respectively), while only a 29% difference was noted between R700 and the commercial catalyst (average Pt particle sizes of 1.3 and 4.6 nm, respectively). This suggests that Pt particles larger than those in this study would perhaps dehydrogenate methanol more readily, but not to a significant extent.

#### *Inter-adsorbate interactions*

The interactions between neighboring surface species, whether similar or different, has been shown to have a strong influence surface species involved in catalytic systems, such as CO on Pt(111) crystals [69,70]. In general, the distribution of CO across the surface, and therefore the nature of adsorbed CO bands, is coverage-dependent. For instance, Krebs and Lüth observed an initial CO<sub>L</sub> band centered at 2068 cm<sup>-1</sup> while probing extremely low CO coverages on Pt(111) [42]. Upon achieving higher (but still low) coverages, the gradual diminishment of this band was proposed to be connected to the rise of a strong band of higher frequency (2079 – 2095 cm<sup>-1</sup>), which remained unchanged when the CO exposure was increased further.

Because this band appeared independently, as opposed to a steady shift of the initial band, it was assigned to the CO<sub>L</sub> stretching mode of adsorbed CO involved in dipole-dipole coupling. The uniformity of site on the Pt(111) single crystal supports the interpretation that this was indeed a coverage effect rather than a kinetic effect due to preferential CO formation on a specific type of site. The same coupling phenomenon seen on Pt single crystals can also occur on Pt nanoparticles.

While increasing CO coverage leads to observable dipole-dipole coupling, it also results in repulsion between species that are directly adjacent [72,73]. Repulsion between adjacent CO species is strongest on Pt terrace sites where the repulsion energy between two adjacent CO species on neighboring Pt atoms (2.77 Å apart) is ~0.05 eV [74]. This results in a lower activation energy for desorption and even the reconstruction or division of large metal terraces and particles [75-79]. This could explain the decreased  $CO_L$  band integral observed for R700 and the Pt/y-Al<sub>2</sub>O<sub>3</sub> commercial catalyst at higher temperatures (Figures 3 and 4). Because the decrease

in the 2079 cm<sup>-1</sup> band for the commercial catalyst was not matched to an observable increase in the band around 2050 cm<sup>-1</sup>, we attribute the smaller CO<sub>L</sub> integrals to desorption rather than migration of adsorbed CO to metal sites of lower coordination.

Time-resolved experiments can provide deeper insight into the most preferred metal sites for dehydrogenation and CO binding. When R500 was first exposed to methanol vapor, the only peak present in the v(C=O) region was located at 2076 cm<sup>-1</sup> which aligns with the primary  $CO_L$  band of the commercial  $Pt/\gamma$ -Al<sub>2</sub>O<sub>3</sub> (Figure 7). At such a low coverage, this early band development matches that in previous studies [42], yet appears to be distinct from the primary band observed in the 2046 – 2052 cm<sup>-1</sup> range at equilibrium. With this there are two possible interpretations. (1) The formation of CO<sub>L</sub> starts on highly coordinated Pt sites. Once these sites are occupied, the band at 2047 cm<sup>-1</sup> becomes dominant shortly after, indicating that subsequently formed CO resides on Pt sites with lower coordination. The largest Pt particles seen on R500 were within the 1.5 - 2 nm, ~10% of the size distribution (Table 1), which are still capable of establishing small Pt terraces and thus CO islands. (2) Following methanol dehydrogenation, adsorbed  $CO_L$  is initially clustered together with a high  $\nu(C\equiv O)$  frequency of 2076 cm-1 (compared the primary 2046 cm<sup>-1</sup> frequency that dominates the spectrum shortly after) resulting in dipole-dipole coupling at low conversion and coverage. Due to the tilting of adsorbed CO on the undercoordinated sites of small Pt particles, we would expect the magnitude of dipole-dipole coupling to be much weaker and have little contribution to the 2076 cm<sup>-1</sup> shoulder. Since CO islands with pronounced dipole-dipole coupling form more easily on larger Pt terraces, it is again suggested that highly coordinated Pt sites are more active methanol dehydrogenation.

Fewer studies have focused on the specific inter-adsorbate forces between adsorbed CO and hydrogen, which is to be expected based on the 4:1 ratio of H\*:CO\* from complete dehydrogenation of methanol. Cheah et al. suggested that repulsion between adjacent CO\* and H\* is somewhat stronger than that of CO\*-CO\* [80]. The repulsion energy between CO\* and H\* on adjacent Pt sites (2.77 Å) can be ~0.11 eV on a Pt(111) surface [81], compared to that of  $\sim 0.05$  eV for CO\*-CO\* repulsion [74]. On Pt/ $\gamma$ -Al<sub>2</sub>O<sub>3</sub>, the two species are either uniformly distributed across the surface or segregated into their own islands. However, given the larger repulsion between CO and H than for CO and CO or H and H, a possible explanation is that the dehydrogenation of methanol on terrace sites is followed by the segregation of these species into their own separate islands. Given the initial 2075 cm<sup>-1</sup> band seen during early exposure of R500 to methanol vapor (Figure 7a), we can expect the initial formation of CO islands to occur on higher coordinate Pt where dehydrogenation also takes place more readily. Concomitantly, surface hydrogen would be pushed outwards towards the nanoparticle edges. There it would either remain bound or leave the metal surface by associative desorption on lowly coordinated Pt [82-85] or reaction with adsorbed oxygen to form H<sub>2</sub>O. To a small extent, hydrogen could spillover onto the  $\gamma$ -Al<sub>2</sub>O<sub>3</sub> support, especially if the support contains defects [86-88]. Any of these phenomena would free up sites for methanol conversion and hence CO formation. As the Pt particles become saturated with CO, they will no longer be able to accommodate further surface species and dehydrogenation activity will slow dramatically. This stagnation can be alleviated by the consumption of adsorbed CO through either desorption, which occurs more readily on larger Pt particles as previously discussed, or the WGS reaction [34,89].

Effects of water

As a solvent for oxygenates and an essential reagent, water is the by far the most abundant component in APR reactors. Consequently, the influence of water on the evolution of relevant intermediate species can have a significant impact on dehydrogenation activity [35]. This may include promoting effects, such as the solvation of surface intermediates or transition states. On the contrary, competitive adsorption can block metal sites needed for the conversion of oxygenates.

Adsorption of water occurred on all Pt/ $\gamma$ -Al $_2$ O $_3$  samples as shown by a strong broad O-H stretching band at 3000 – 3500 cm $^{-1}$  and a medium H-O-H scissoring deformation band centered at 1646 cm $^{-1}$  (Figure S5). The Lewis acid sites of  $\gamma$ -Al $_2$ O $_3$  have a particularly strong affinity to water [90]. At increased temperatures, formation of a boehmite phase with decreased acidity is expected unless the alumina is stabilized [90-95].

The appearance of adsorbed CO stretching bands on hydrated catalyst surfaces suggest methanol dehydrogenation still occurs under the presence of co-adsorbed water. A few observations from the kinetic experiments (Figure 7) in particular can provide insight to the effects of water. First, the increase in integrals of the CO<sub>L</sub> and CO<sub>B</sub> bands appear to be in sync and equilibrate at the same time (30 min for small Pt particles and ~1 min for large Pt particles). On a dry Pt terrace, the fraction of CO<sub>B</sub> is known to be coverage-dependent [97]. As coverage increases, CO species transition from isolation to islands where CO<sub>B</sub> formation begins due to dipole-dipole coupling [42]. Yet, CO<sub>B</sub> appears to be present at low CO coverages in all experiments with and without water. In addition, the presence of CO<sub>B</sub> is largely amplified on

small Pt particles when they are hydrated with H<sub>2</sub>O (Figure 7b) but not on large, hydrated Pt particles (Figure 7d) where islands form more easily on larger terraces. The primary frequency even decreased about 10 cm<sup>-1</sup> over 5 minutes, suggesting that the extent of dipole-dipole coupling decreases due to the instability of CO islands. These points together suggest that the majority of adsorbed CO resulting from methanol dehydrogenation intermixes with co-adsorbed H<sub>2</sub>O rather than segregating into separate islands. A similar conclusion was reached by Kizhakevariam et al. when modeling CO/H<sub>2</sub>O co-adsorption on Pt electrode interfaces [98]. This suggests that changes in the CO stretching bands are dominated by the electronic and chemical effects of co-adsorbed H<sub>2</sub>O and a concomitant reorganization of adsorbed CO on Pt sites.

With co-adsorbed water present, the initial rate of methanol dehydrogenation over R500 (Figure 7b) was reduced significantly. It took about 5 min for discernable, yet still weak, CO bands to appear while CO formation on the commercial catalyst seemed virtually unaffected (Figure 7d). This suggests that the presence of co-adsorbed water is detrimental to the dehydrogenation reaction on small Pt particles, or uncoordinated Pt sites. We believe this to be in part due to hindered adsorption of methanol to sites currently occupied by H<sub>2</sub>O. It is known that H<sub>2</sub>O has a higher binding energy on Pt sites with lower coordination [99]. We expect this to also hold true for the small Pt particles of R500.

As a ligand, water is expected to increase the electron density of nearby metal centers and chemical nature of adjacent CO [50,51]. This would improve the back bonding into the CO  $\pi^*$  LUMO, thus decreasing the  $\nu$ (C=O) frequency. In addition, a decrease in the catalyst acidity due to the partial hydration of  $\gamma$ -Al<sub>2</sub>O<sub>3</sub> into boehmite might decrease the Fermi level of

supported Pt atoms [100]. This effect increases the availability of electrons near the d-band edge. These phenomena simultaneously improves the ability for Pt to back donate into the CO  $\pi^*$  molecular orbital, thus reducing the C=O bond strength [101]. This is reflected by a red shift of the v(C=O) band [51]; more so on R700 and the commercial catalyst which demonstrated methanol conversion at low temperatures with (2045 and 2073 cm<sup>-1</sup>, respectively, at 150 °C) and without adsorbed water (2050 and 2081 cm<sup>-1</sup>, respectively, at 150 °C). This effect, seen here under UHV conditions, is further amplified during APR using liquid flow as previously witnessed [59,60]. Solvation of adsorbed CO by H<sub>2</sub>O is also possible because APR occurs in bulk water. Solvation involves intermolecular interactions between the surface species and the solvent that can ultimately affect the energetics of the reaction; oxidation via the water-gas shift reaction in this case. For adsorbed CO, multiple studies claimed that the red shift of CO stretching bands is evidence for the solvation of adsorbed CO [50,51,98]. This is most evident on small Pt particles (Figure 7a,b) where solvation by H<sub>2</sub>O may also contribute to differences in the CO<sub>B</sub> band integral on a hydrated catalyst surface. The CO<sub>B</sub> frequency range was about 1730 - 1880 and 1700 - 1850 cm<sup>-1</sup> for dry and hydrated R500, respectively. We suspect a combination of both electronic and chemical effects cause these changes in the CO bands.

While the  $H_2O$ -induced promotion of  $CO_B$ , the active intermediate in the WGS reaction, was evident only on small Pt particles, we speculate that this would not outweigh the consequences of decreased dehydrogenation rates and that larger Pt particles may still prove to be more active for the overall APR reaction.

# Conclusion

Renewable hydrogen production via aqueous phase reforming (APR) is initiated by alcohol dehydrogenation of cellulosic biomass-derived oxygenates. The catalysis fundamentals behind this reaction are isolated by observing methanol conversion on Pt/y-Al<sub>2</sub>O<sub>3</sub> using infrared spectroscopy under high vacuum with and without co-adsorbed H<sub>2</sub>O. Evolution of the resulting CO stretching bands, linear CO (CO<sub>L</sub>) at  $1920 - 2140 \text{ cm}^{-1}$  and bridging CO (CO<sub>B</sub>) at 1750 - 1800cm<sup>-1</sup>, are deconvoluted to determine the preferred surface environment for high dehydrogenation activity. The kinetic experiments in which large Pt particles achieved equilibrium conversion within a minute while small Pt particles required about 30 minutes suggest that terrace sites are more active for complete dehydrogenation of methanol than undercoordinated sites. Larger v(C≡O) bands were also observed for the catalyst with larger Pt particles as low as 50 °C in temperature-programmed experiments. Even on smaller Pt particles, methanol appears to dehydrogenate on the metal sites of highest coordination first. The presence of water amplifies the presence of CO<sub>B</sub> but impedes the rate of methanol dehydrogenation on small Pt particles below 250 °C perhaps due to strongly bound water on lowly coordinated Pt, especially near the metal/support interface. Continuing efforts in studying the catalysis fundamentals of aqueous phase reforming will permit improved reaction efficiency and acquisition of renewable hydrogen.

# **Acknowledgements**

This project was funded by the National Science Foundation through grants number CHE-1764304 and CHE-1764296. Yong Ding and Qandeel Almas are thanked for assistance with

STEM imaging and XPS data acquisition, respectively. The STEM and XPS experiments were performed in part at the Georgia Tech Institute for Electronics and Nanotechnology, a member of the National Nanotechnology Coordinated Infrastructure, which is supported by the National Science Foundation (Grant ECCS-1542174).

# References

- [1] C.-J. Winter, International Journal of Hydrogen Energy 34 (2009) S1.
- [2] T.N. Veziroğlu, S. Şahi, Energy Conversion and Management 49 (2008) 1820.
- [3] V. Piemonte, M. Capocelli, G. Orticello, L. Di Paola, Membrane Technologies for Biorefining, Elsevier. 263.
- [4] Y. Tanabe, Y. Nishibayashi, Coord. Chem. Rev. 257 (2013) 2551.
- [5] A.Y. Krylova, Solid Fuel Chemistry 48 (2014) 22.
- [6] E. Taibi, R. Miranda, W. Vanhoudt, T. Winkel, J.-C. Lanoix, F. Barth. 2018. Hydrogen From Renewable Power: Technology Outlook for the Energy Transition. I.R.E. Agency, editor, Abu Dhabi.
- [7] H. Balat, E. Kırtay, International Journal of Hydrogen Energy 35 (2010) 7416.
- [8] G.W. Huber, S. Iborra, A. Corma, Chemical Reviews 106 (2006) 4044.
- [9] E. Kirtay, Energy Conversion & Management 52 (2011) 1778.
- [10] R.D. Cortright, R.R. Davda, J.A. Dumesic, Nature 418 (2002) 964.
- [11] G.W. Huber, J.A. Dumesic, Catalysis Today 111 (2006) 119.
- [12] R.R. Davda, J.A. Dumesic, Chemical Communications (2004) 36.
- [13] G. Wen, Y. Xu, H. Ma, Z. Xu, Z. Tian, International Journal of Hydrogen Energy 33 (2008) 6657.
- [14] R.R. Davda, J.W. Shabaker, G.W. Huber, R.D. Cortright, J.A. Dumesic, Applied Catalysis B: Environmental 56 (2005) 171.
- [15] Y.-B. Huang, Y. Fu, Green Chemistry 15 (2013) 1095.
- [16] I. Coronado, M. Stekrova, M. Reinikainen, P. Simell, L. Lefferts, J. Lehtonen, Internation Journal of Hydrogen Energy 41 (2016) 11003.
- [17] P.D. Vaidya, J.A. Lopez-Sanchez, ChemistrySelect 2 (2017) 6563.
- [18] D.A. Cantero, Á. Sánchez Tapia, M.D. Bermejo, M.J. Cocero, Chem. Eng. J. 276 (2015) 145.
- [19] A. Ciftci, S. Eren, D.A.J.M. Ligthart, E.J.M. Hensen, ChemCatChem 6 (2014) 1260.
- [20] T.-W. Kim, H.J. Park, Y.-C. Yang, S.-Y. Jeong, C.-U. Kim, International Journal of Hydrogen Energy 39 (2014) 11509.
- [21] H.-D. Kim, H.J. Park, T.-W. Kim, K.-E. Jeong, H.-J. Chae, S.-Y. Jeong, C.-H. Lee, C.-U. Kim, International Journal of Hydrogen Energy 37 (2012) 8310.

- [22] G.W. Huber, J.W. Shabaker, S.T. Evans, J.A. Dumesic, Applied Catalysis B: Environmental 62 (2006) 226.
- [23] T. Sakamoto, T. Miyao, A. Yoshida, S. Naito, International Journal of Hydrogen Energy 35 (2010) 6203.
- [24] N. Luo, X. Fu, F. Cao, T. Xiao, P.P. Edwards, Fuel 87 (2008) 3483.
- [25] N.D. Subramanian, J. Callison, C.R.A. Catlow, P.P. Wells, N. Dimitratos, International Journal of Hydrogen Energy 41 (2016) 18441.
- [26] M.F. Neira D'Angelo, V. Ordomsky, J. van der Schaaf, J.C. Schouten, T.A. Nijhuis, Catalysis Science & Technology 3 (2013) 2834.
- [27] M.F. Neira D'Angelo, V. Ordomsky, J. van der Schaaf, J.C. Schouten, T.A. Nijhuis, International Journal of Hydrogen Energy 39 (2014) 18069.
- [28] K. Lehnert, P. Claus, Catalysis Communications 9 (2008) 2543.
- [29] H. Pines, J. Manassen, in: D.D. Eley, H. Pines, P.B. Weisz, (Eds.), Advances in Catalysis, Academic Press. 49.
- [30] Q. Zhang, W. Deng, Y. Wang, Chemical communications 47 (2011) 9275.
- [31] A. Friedrich, S. Schneider, ChemCatChem 1 (2009) 72.
- [32] T. Mitsudome, Y. Mikami, H. Funai, T. Mizugaki, K. Jitsukawa, K. Kaneda, Angewandte Chemie International Edition 47 (2008) 138.
- [33] W. Fang, Q. Zhang, J. Chen, W. Deng, Y. Wang, Chemical communications 46 (2010) 1547.
- [34] T. Xie, B.J. Hare, P.J. Meza-Morales, C. Sievers, R.B. Getman, Journal of Physical Chemistry C 124 (2020) 19015.
- [35] C. Sievers, Y. Noda, L. Qi, E.M. Albuquerque, R.M. Rioux, S.L. Scott, ACS Catalysis 6 (2016) 8286.
- [36] M. Saleheen, A. Heyden, ACS Catalysis 8 (2018) 2188.
- [37] J.M. Kim, R. Ryoo, Bull. Korean Chem. Soc. 17 (1996) 66.
- [38] S. Brunauer, P.H. Emmett, E. Teller, Journal of the American Chemical Society 60 (1938) 309.
- [39] M. Tamura, K.-i. Shimizu, A. Satsuma, Applied Catalysis A: General 433 (2012) 135.
- [40] X. Liu, R.E. Truitt, Journal of the American Chemical Society 119 (1997) 9856.
- [41] G. Busca, P.F. Rossi, V. Lorenzelli, M. Benaissa, J. Travert, J.C. Lavalley, The Journal of Physical Chemistry 89 (1985) 5433.
- [42] H.-J. Krebs, H. Lüth, Applied physics 14 (1977) 337.
- [43] M.J. Kappers, J.H. van der Maas, Catalysis Letters 10 (1991) 365.
- [44] M. Kappers, J. Miller, D. Koningsberger, The Journal of Physical Chemistry 100 (1996) 3227.
- [45] R. Barth, A. Ramachandran, J. Catal. 125 (1990) 467.
- [46] P. Deshlahra, J. Conway, E.E. Wolf, W.F. Schneider, Langmuir 28 (2012) 8408.
- [47] K. Ding, A. Gulec, A.M. Johnson, N.M. Schweitzer, G.D. Stucky, L.D. Marks, P.C. Stair, Science 350 (2015) 189.
- [48] C. Dessal, T. Len, F. Morfin, J.-L. Rousset, M. Aouine, P. Afanasiev, L. Piccolo, ACS Catalysis 9 (2019) 5752.
- [49] Y. Zhao, L. Wang, A. Kochubei, W. Yang, H. Xu, Y. Luo, A. Baiker, J. Huang, Z. Wang, Y. Jiang, The Journal of Physical Chemistry Letters 12 (2021) 2536.

- [50] S.D. Ebbesen, B.L. Mojet, L. Lefferts, Journal of Catalysis 246 (2007) 66.
- [51] B.L. Mojet, S.D. Ebbesen, L. Lefferts, Chemical Society Reviews 39 (2010) 4643.
- [52] G. Germani, Y. Schuurman, AIChE Journal 52 (2006) 1806.
- [53] Y. Amenomiya, Journal of Catalysis 57 (1979) 64.
- [54] A. Goguet, F.C. Meunier, D. Tibiletti, J.P. Breen, R. Burch, Journal of Physical Chemistry B 108 (2004) 20240.
- [55] F.T. Wagner, T.E. Moylan, S.J. Schmieg, Surface Science 195 (1988) 403.
- [56] M. Weller, T. Overton, J. Rourke, F. Armstrong, Inorganic Chemistry. Oxford University Press, New York, NY 10016, United States of America, 2018.
- [57] M.A. Vannice, C.C. Twu, The Journal of Chemical Physics 75 (1981) 5944.
- [58] B. Beden, A. Bewick, K. Kunimatsu, C. Lamy, J. Electroanal. Chem. 142 (1982) 345.
- [59] J.R. Copeland, G.S. Foo, L.A. Harrison, C. Sievers, Catalysis Today 205 (2013) 49.
- [60] J. So, Y. Chung, D.S. Sholl, C. Sievers, Mol. Catal. 475 (2019) 110423.
- [61] A. Garnier, S. Sall, F. Garin, M.J. Chetcuti, C. Petit, Journal of Molecular Catalysis A: Chemical 373 (2013) 127.
- [62] P. Hollins, Surface Science 16 (1992) 51.
- [63] P. Hollins, J. Pritchard, Progress in Surface Science 19 (1985) 275.
- [64] R. Queau, D. Labroue, R. Poilblanc, Journal of Catalysis 69 (1981) 249.
- [65] A.B. Anderson, M.K. Awad, Journal of the American Chemical Society 107 (1985) 7854.
- [66] B. Qiao, A. Wang, X. Yang, L.F. Allard, Z. Jiang, Y. Cui, J. Liu, J. Li, T. Zhang, Nature Chemistry 3 (2011) 634.
- [67] A. Ciftci, D.A.J.M. Ligthart, E.J.M. Hensen, Applied Catalysis B: Environmental 174-175 (2015) 126.
- [68] R.A. Van Santen, ACCOUNTS OF CHEMICAL RESEARCH 42 (2009) 57.
- [69] C.W. Olsen, R.I. Masel, Surface Science 201 (1988) 444.
- [70] M. Tüshaus, E. Schweizer, P. Hollins, A. Bradshaw, Journal of electron spectroscopy and related phenomena 44 (1987) 305.
- [71] G. Ertl, M. Neumann, K. Streit, Surface Science 64 (1977) 393.
- [72] R. Raval, S. Haq, M. Harrison, G. Blyholder, D. King, Chemical physics letters 167 (1990) 391.
- [73] R. Brako, D. Šokčević, Surface science 401 (1998) L388.
- [74] N.V. Petrova, I.N. Yakovkin, Surface Science 519 (2002) 90.
- [75] A. Myshlyavtsev, V. Zhdanov, Langmuir 9 (1993) 1290.
- [76] P. Hofmann, S.R. Bare, D.A. King, Surface Science 117 (1982) 245.
- [77] F. Tao, S. Dag, L.-W. Wang, Z. Liu, D.R. Butcher, H. Bluhm, M. Salmeron, G.A. Somorjai, Science 327 (2010) 850.
- [78] R. Behm, P. Thiel, P. Norton, G. Ertl, The Journal of Chemical Physics 78 (1983) 7437.
- [79] P. van Beurden, H. Verhoeven, G. Kramer, B. Thijsse, Physical review B 66 (2002) 235409.
- [80] S.K. Cheah, V.r.P. Bernardet, A.A. Franco, O. Lemaire, P. Gelin, The Journal of Physical Chemistry C 117 (2013) 22756.
- [81] T. Roman, H. Nakanishi, H. Kasai, Physical Chemistry Chemical Physics 10 (2008) 6052.
- [82] P. Zhou, H. Zhang, H. Ji, W. Ma, C. Chen, J. Zhao, Science China Chemistry 63 (2020) 354.
- [83] G.-F. Wei, Z.-P. Liu, Chemical science 6 (2015) 1485.

- [84] R. Kajiwara, Y. Asaumi, M. Nakamura, N. Hoshi, Journal of electroanalytical chemistry 657 (2011) 61.
- [85] S. Gudmundsdóttir, E. Skúlason, H. Jónsson, Physical review letters 108 (2012) 156101.
- [86] F. Modica, J. Miller, B. Meyers, D. Koningsberger, Catalysis today 21 (1994) 37.
- [87] M. Stoica, M. Caldararu, F. Rusu, N. Ionescu, Applied Catalysis A: General 183 (1999) 287.
- [88] W. Karim, C. Spreafico, A. Kleibert, J. Gobrecht, J. VandeVondele, Y. Ekinci, J.A. van Bokhoven, Nature 541 (2017) 68.
- [89] B.S. RJ, M. Loganathan, M.S. Shantha, International Journal of Chemical Reactor Engineering 8 (2010).
- [90] R.M. Ravenelle, J.R. Copeland, W.-G. Kim, J.C. Crittenden, C. Sievers, ACS Catalysis 1 (2011) 552.
- [91] A. Ciftci, B. Peng, A. Jentys, J.A. Lercher, E.J. Hensen, Applied Catalysis A: General 431 (2012) 113.
- [92] K. Koichumanova, K.S.S. Gupta, L. Lefferts, B. Mojet, K. Seshan, Physical chemistry chemical physics 17 (2015) 23795.
- [93] P. Nortier, P. Fourre, A.B.M. Saad, O. Saur, J.C. Lavalley, Applied Catalysis 61 (1990) 141.
- [94] Y. Men, H. Gnaser, C. Ziegler, Analytical and Bioanalytical Chemistry 375 (2003) 912.
- [95] D.D. MacDonald, P. Butler, Corrosion Science 13 (1973) 259.
- [96] P. Liu, J.A. Rodriguez, The Journal of Chemical Physics 126 (2007) 164705.
- [97] M. Tüshaus, W. Berndt, H. Conrad, A.M. Bradshaw, B. Persson, Appl. Phys. A 51 (1990) 91.
- [98] N. Kizhakevariam, X. Jiang, M.J. Weaver, Journal of Chemical Physics 100 (1994) 6750.
- [99] A. den Dunnen, M.J. van der Niet, C. Badan, M.T. Koper, L.B. Juurlink, Physical Chemistry Chemical Physics 17 (2015) 8530.
- [100] B.L. Mojet, J.T. Miller, D.E. Ramaker, D.C. Koningsberger, Journal of Catalysis 186 (1999) 373.
- [101] R.A. van Santen, Journal of the Chemical Society, Faraday Transactions 1: Physical Chemistry in Condensed Phases 83 (1987) 1915.